AIMS Energy, 9(3): 465–482.
DOI: 10.3934/energy.2021023
Received: 28 December 2020
Accepted: 05 April 2021
Published: 09 April 2021

http://www.aimspress.com/journal/energy

Research article

Thermodynamic performance of near-field electroluminescence and negative electroluminescent refrigeration systems

Bowen Li, Qiang Cheng*, Jinlin Song, Kun Zhou, Lu Lu and Zixue Luo

State Key Laboratory of Coal Combustion, School of Energy and Power Engineering, Huazhong University of Science and Technology, Wuhan 430074, Hubei, China

* **Correspondence:** Email: chengqiang@mail.hust.edu.cn.

Abstract: Electroluminescent (EL) and negative electroluminescent (NEL) devices are radiative thermoelectric energy converters that use electric power for refrigeration. For the EL system, we apply a forward bias to the emitter that we want to cool, whereas a reverse bias voltage is applied to the hot absorber for the NEL system. In this work, we derive the thermodynamic limits of the cooling power density and coefficient of performance (COP) of near-field EL and NEL refrigeration systems based on entropy analysis that considers near-field effects. We show numerically that operating the EL and NEL systems in the near-field regime could increase the cooling power density and the COP bounds to a certain extent. As the vacuum gap decrease from 1000 to 10 nm, the near-field effects improve the performance of the NEL system all the time, but the performance of the EL system increases to the optimal value and then decreases. In addition, the increase in temperature difference weakens the performance of both refrigeration systems greatly. Moreover, we also investigate the effects of the absence of sub-bandgap thermal radiation on the performance of the EL and NEL systems. Our work indicates significant opportunities for evaluating the performance of near-field radiative thermoelectric energy converters from the perspective of thermodynamic limits. Meanwhile, these results establish the targets for cooling power density and COP of the near-field EL and NEL systems.

Keywords: near-field radiative transfer; electroluminescent; negative electroluminescent; entropy; thermodynamic bounds

1. Introduction

In the near-field, the radiative heat transfer could be enhanced by several orders of magnitude as compared to the Planck's blackbody limit due to the presence of evanescent waves [1–9]. In recent years, this enhancement has been experimentally demonstrated [8–14]. Such enhancement has been widely studied in many applications like energy conversion systems [15–22]. Moreover, there has been growing interest in active control of near-field heat transfer like electroluminescent (EL) [23–25] and negative electroluminescent (NEL) refrigeration [26–28].

In most of the previous work on the near-field radiative heat transfer, it is assumed that the chemical potential of the object involved is zero. However, when photons are in quasiequilibrium with semiconductors under external bias, they can have a chemical potential [29]. One approach to operating a semiconductor *p-n* junction as an EL refrigeration device is to apply a forward bias to make the body emit excess photons and cool down below ambient temperature [30].

The first prediction of EL refrigeration was made by Tuac in 1957 [31], then this evidence was achievable by Dousmanis et al. in 1963 [32]. Compared with traditional solid-state thermoelectric refrigerators, this refrigeration approach has many special superiorities, such as higher efficiency, easier integration with other optoelectronic devices, and wider operating temperatures [24]. In the past few decades, there have been some studies expounding on the potential of EL refrigeration [33–38]. Recently, the electroluminescence refrigeration effect was experimentally demonstrated for narrow bandgap emitters under an ultralow applied bias [39].

Due to the quite low cooling power density of far-field EL cooling devices, the concept of near-field electromagnetic heat transfer can be used to enhance the performance of EL refrigeration. In 2012, Guha et al. [40] experimentally demonstrated the efficient EL refrigeration and theoretically proved that it is feasible to realize very strong cooling in the near-field regime. Chen et al. [23] first theoretically investigated the near-field EL refrigeration considering contributions of evanescent waves and phonon modes in 2015. They predicted that refrigeration effects can occur between two semiconductor bodies when the gap spacing ranges from tens to hundreds of nanometers. Liu and Zhang [24] developed a multilayer model to consider the nonuniform distribution of the chemical potential of photons and nanoscale radiative transfer.

In addition to the EL effect of the forward-biased *p-n* junction, the reverse-biased junction can also achieve refrigeration through the NEL effect [41–44]. This effect was demonstrated experimentally by Ashley et al. [45] for reverse-biased InSb and mercury cadmium telluride (MCT) diodes. Chen et al. [26] analyzed the near-field enhanced NEL, for an ideal narrow-band-gap semiconductor, they show that power density can be increased significantly and the efficiency can be close to the Carnot limit in the near-field regime. Then Zhu et al. [46] firstly reported an experimental demonstration of near-field NEL refrigeration using a nanocalorimetric device and a photodiode. Very recently, Zhou et al. [28] theoretically analyze the performance of a near-field NEL refrigeration system consisting of a Mie-metamaterial emitter.

With the consideration of the near-field effect, the influence on the maximum active work and energy conversion efficiency of the EL and NEL systems should be concerned. Moreover, entropy plays a key role in the determination of the thermodynamic limit of the maximum work and the energy conversion efficiency [47–52]. In the near-field regime, Dorofeyev first studied the energy and entropy density due to near-field effects in equilibrium at the interface [53]. The maximum work and the upper bound for the efficiency of thermal radiation have been obtained by Perez-Madrid et al. [54–56].

Moreover, in consideration of both near-field effects and the condition of thermal nonequilibrium, Narayanaswamy and Zheng [57] derived a method to obtain the maximum work and the energy conversion efficiency limit in near-field thermal radiation. Recently, this method was applied to the performance evaluation of near-field thermophotovoltaic systems [58].

In the present work, we derive thermodynamic bounds for the cooling power densities and the coefficient of performance (COP) of the near-field EL and NEL systems by calculating the radiative heat flux and entropy flux that considers near-field effects. Then we present the performance of the near-field EL and NEL systems at different vacuum gaps. Furthermore, the effects of the temperature difference and sub-bandgap thermal radiation on the thermodynamic performance are thoroughly investigated.

2. The configuration and formalism

2.1. Geometry and materials

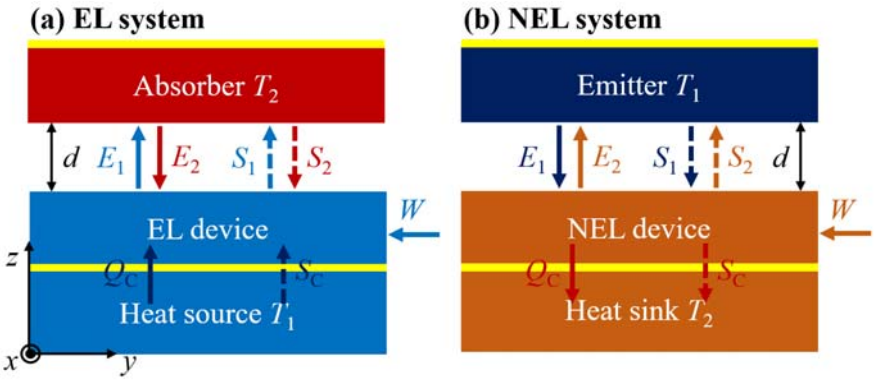

Figure 1. Schematic and energy flow diagram of a near-field (a) EL and (b) NEL system. The EL system consists of three bodies, i.e., heat source, EL device (emitter), and absorber. The NEL system consists of an emitter, NEL device (absorber), and heat sink. The emitter and absorber are enclosed within two Au substrates.

The considered configurations of the near-field EL and NEL systems to be investigated in this study are schematically shown in Figure 1. A near-field EL energy conversion system consists of a heat source (cooling target), an EL *p*-*n* device as an emitter, and an absorber. Where the vacuum gap spacing between the emitter and absorber is denoted by d. The emitter and absorber are enclosed within Au substrates acting as perfect mirrors at the top and bottom boundaries respectively, as shown by the yellow layers. The structure of a NEL system is similar to that of an EL system, as shown in Figure 1(b). The difference is that the NEL device acts as an absorber. This work focuses on the near-field radiative transfer so that we assume ideal thermal contact between the different layers.

Then we briefly review the concept of EL and NEL refrigeration. In the case where the EL device is colder than the absorber. By supplying with electrical work as delivered by an external forward voltage V_{EL}, a near-field EL device emits an increased number of photons as compared to the same material under equilibrium conditions, and some of this photon energy is derived from the

thermal energy of the lattice. Under an adequate high operating voltage, such an increased photon emission can result in a net heat flux pumped from a cold EL device to a hot absorber in spite of the fact that the EL device has a lower temperature. As for a NEL device under a reverse bias voltage (i.e., $V_{\mathrm{NEL}} < 0$), the photon emission decreases, it can extract a net radiative heat flux from an emitter (cooling target) with a lower temperature. Hence the resulting structures shown in Figure 1 can be used for refrigeration purposes.

In the calculation, the thicknesses of emitter and absorber denoted as d_1 and d_2 are chosen to be 5 μm to ensure significant emission and absorption. For a fair comparison between the EL and NEL systems, the temperatures of the two heat reservoirs are fixed. The cooling target temperatures (that is, the temperatures of the heat source of the EL system and the emitter of the NEL system) are maintained at a low-temperature T_1, whereas the absorber of the EL system and the heat sink of the NEL system are maintained at a high-temperature $T_2 = 300$ K. In the near-field EL system, we choose InAs as the semiconductor for both the absorber and EL device, whose bandgap energy E_{g} is 0.354 eV at room temperature [59]. For the near-field NEL system, we use a narrow band-gap semiconductor MCT as the NEL device and emitter. It has a bandgap of $E_{\mathrm{g}} = 0.169$ eV [26]. The optical constants of InAs and MCT are taken from Ref. [60]. Moreover, the dielectric function of Au as a function of angular frequency ω, is approximated by the Drude model [61]: $\varepsilon_{\mathrm{Au}}(\omega) = 1 - \omega_{\mathrm{p}}^2/(\omega^2 + i\gamma\omega)$ with a plasma frequency $\omega_{\mathrm{p}} = 1.37 \times 10^{16}$ rad/s and damping rate $\gamma = 7.31 \times 10^{13}$ rad/s.

2.2. Calculation of near-field radiative transfer

The energy flows (solid arrows) and entropy flows (dashed arrows) of the near-field EL and NEL systems are shown in Figure 1. An EL device absorbs net outflux of heat Q_{C} and entropy S_{C} from the cold heat source in the form of heat conduction. Then by the injected electric power W, the EL device pumps heat flux ($E_1 - E_2$) and entropy flux ($S_1 - S_2$) to the hot absorber via near-field radiation. As for a NEL system, the biased NEL device absorbs heat flux ($E_1 - E_2$) and entropy flux ($S_1 - S_2$) from the cold emitter and rejects heat flux Q_{C} and entropy flux S_{C} to the hot heat sink.

The polarized radiative heat flux ($E_1 - E_2$) between two bodies has contributions both from sub-bandgap frequency components ($E_{1,\mathrm{s}} - E_{2,\mathrm{s}}$) due to phonon-polariton excitations, and from above-bandgap frequency components ($E_{1,\mathrm{a}} - E_{2,\mathrm{a}}$) due to electronic excitations. Using the fluctuation-dissipation theorem [62–64], the radiative heat flux can be expressed as

$$\begin{aligned} E_{1,\mathrm{s}}^{(j)} - E_{2,\mathrm{s}}^{(j)} = \int_0^{\omega_g/c} \hbar\omega dk_0 \Bigg\{ \int_0^{k_0}\int_0^{2\pi} \left[n_1^{(j)}(0)\upsilon_1^{(j)} - n_2^{(j)}(0)\upsilon_2^{(j)} \right] k_0/\left|k_{z0}\right| dk_\rho k_\rho d\phi \\ + \int_{k_0}^{\infty}\int_0^{2\pi} \left[n_1^{(j)}(0)\upsilon_1^{(j)} - n_2^{(j)}(0)\upsilon_2^{(j)} \right] \sqrt{\beta_{z0}^2 + k_\rho^2}/\left|\beta_{z0}\right| dk_\rho k_\rho d\phi \Bigg\}, \end{aligned} \tag{1a}$$

$$\begin{aligned} E_{1,\mathrm{a}}^{(j)} - E_{2,\mathrm{a}}^{(j)} = \int_{\omega_g/c}^{+\infty} \hbar\omega dk_0 \Bigg\{ \int_0^{k_0}\int_0^{2\pi} \left[n_1^{(j)}(V_1)\upsilon_1^{(j)} - n_2^{(j)}(V_2)\upsilon_2^{(j)} \right] k_0/\left|k_{z0}\right| dk_\rho k_\rho d\phi \\ + \int_{k_0}^{\infty}\int_0^{2\pi} \left[n_1^{(j)}(V_1)\upsilon_1^{(j)} - n_2^{(j)}(V_2)\upsilon_2^{(j)} \right] \sqrt{\beta_{z0}^2 + k_\rho^2}/\left|\beta_{z0}\right| dk_\rho k_\rho d\phi \Bigg\}. \end{aligned} \tag{1b}$$

Here, $j = s, p$ accounts for the polarization states, ω_{g} is the band-gap frequency of the semiconductor defined as $\omega_{\mathrm{g}} = E_{\mathrm{g}}/\hbar$, $\hbar$ is the reduced Planck constant, V denotes the applied voltage. For the EL system, $V_1 > 0$ and $V_2 = 0$; For the NEL system, $V_1 = 0$ and $V_2 < 0$. We note that Eq (1a) and (1b) contain triple integrations over the azimuthal angle ϕ, the component of the

wavevector on the x-y plane k_ρ, and the free-space wavevector $k_0 = \omega/c$ with c being the speed of light in vacuum. The wavevectors component in the z-direction for propagating waves (PW) and evanescent waves (EW) are expressed as $k_{z0} = \sqrt{k_0^2 - k_\rho^2}$ and $\beta_{z0} = \sqrt{k_\rho^2 - k_0^2}$, respectively. Moreover, $n_h^{(j)}(V)$ is the number of emitted photons with $h = 1, 2$, and $\upsilon_h^{(j)}$ is the z component of the local velocity of the energy transmission. Further, $n_h^{(j)}(V)$ and $\upsilon_h^{(j)}$ are respectively defined as

$$n_h^{(j)}(V) = \begin{cases} \dfrac{\mathrm{sgn}(k_{z0})}{8\pi^3 f_h(V)} \dfrac{(1-\left|R_h^{(j)}\right|^2)[1+\left|R_{\bar{h}}^{(j)}\right|^2 + \dfrac{k_\rho^2}{k_0^2} 2\,\mathrm{Re}(R_{\bar{h}}^{(j)} e^{i2k_{z0}d_{\bar{h}}})]}{\left|1 - R_h^{(j)} R_{\bar{h}}^{(j)} e^{i2k_{z0}d}\right|^2} & \text{for PW,} \\ \dfrac{\mathrm{sgn}(\beta_{z0})}{8\pi^3 f_h(V)} \dfrac{k_0}{\sqrt{\beta_{z0}^2 + k_\rho^2}} \dfrac{2\,\mathrm{Im}(R_h^{(j)}) e^{-2\beta_{z0}d}}{\left|1 - R_h^{(j)} R_{\bar{h}}^{(j)} e^{-2\beta_{z0}d}\right|^2} & \text{for EW,} \\ \times[2\,\mathrm{Re}(R_{\bar{h}}^{(j)}) + \dfrac{k_\rho^2}{k_0^2}(e^{2\beta_{z0}d_{\bar{h}}} + e^{-2\beta_{z0}d_{\bar{h}}} \left|R_{\bar{h}}^{(j)}\right|^2)] & \end{cases} \tag{2}$$

$$\upsilon_h^{(j)} = \begin{cases} \dfrac{ck_{z0}}{k_0} \dfrac{\dfrac{1-\left|R_{\bar{h}}^{(j)}\right|^2}{1+\left|R_{\bar{h}}^{(j)}\right|^2}}{1 + \dfrac{k_\rho^2}{k_0^2} \dfrac{2\,\mathrm{Re}(R_{\bar{h}}^{(j)} e^{i2k_{z0}d_{\bar{h}}})}{1+\left|R_{\bar{h}}^{(j)}\right|^2}} & \text{for PW,} \\ \dfrac{c\beta_{z0}k_0}{k_\rho^2} \dfrac{\dfrac{2\,\mathrm{Im}(R_{\bar{h}}^{(j)}) e^{-2\beta_{z0}d_{\bar{h}}}}{1+\left|R_{\bar{h}}^{(j)}\right|^2 e^{-4\beta_{z0}d_{\bar{h}}}}}{1 + \dfrac{k_0^2}{k_\rho^2} \dfrac{2\,\mathrm{Re}(R_{\bar{h}}^{(j)}) e^{-2\beta_{z0}d_{\bar{h}}}}{1+\left|R_{\bar{h}}^{(j)}\right|^2 e^{-4\beta_{z0}d_{\bar{h}}}}} & \text{for EW,} \end{cases} \tag{3}$$

where $d_h = \left|z - z_h\right|$, $\bar{h} = 2$ if $h = 1$, and vice versa. $f_h(V) = [e^{(\hbar\omega - qV)/k_B T_h} - 1]^{-1}$ is the photon distribution function, k_B is the Boltzmann constant and q is the magnitude of the electron's charge. We define $R_h^{(j)}$ as the reflection coefficients from vacuum to body h for j polarization with Au substrates [65,66].

The entropy flux carried by the related energy flux [Eq (1)] takes the form

$$\begin{aligned} S_{1,\mathrm{s}}^{(j)} - S_{2,\mathrm{s}}^{(j)} = \int_0^{\omega_g/c} d\omega \Bigg\{ & \int_0^{k_0} \int_0^{2\pi} \left[s_1^{(j)}(0)\upsilon_1^{(j)} - s_2^{(j)}(0)\upsilon_2^{(j)} \right] k_0 / \left|k_{z0}\right| dk_\rho k_\rho d\phi \\ & + \int_{k_0}^{\infty} \int_0^{2\pi} \left[s_1^{(j)}(0)\upsilon_1^{(j)} - s_2^{(j)}(0)\upsilon_2^{(j)} \right] \sqrt{\beta_{z0}^2 + k_\rho^2} / \left|\beta_{z0}\right| dk_\rho k_\rho d\phi \Bigg\}, \end{aligned} \tag{4a}$$

$$\begin{aligned} S_{1,\mathrm{a}}^{(j)} - S_{2,\mathrm{a}}^{(j)} = \int_{\omega_g/c}^{+\infty} d\omega \Bigg\{ & \int_0^{k_0} \int_0^{2\pi} \left[s_1^{(j)}(V_1)\upsilon_1^{(j)} - s_2^{(j)}(V_2)\upsilon_2^{(j)} \right] k_0 / \left|k_{z0}\right| dk_\rho k_\rho d\phi \\ & + \int_{k_0}^{\infty} \int_0^{2\pi} \left[s_1^{(j)}(V_1)\upsilon_1^{(j)} - s_2^{(j)}(V_2)\upsilon_2^{(j)} \right] \sqrt{\beta_{z0}^2 + k_\rho^2} / \left|\beta_{z0}\right| dk_\rho k_\rho d\phi \Bigg\}, \end{aligned} \tag{4b}$$

with the near-field entropy density s_h given by [57]

$$s_h^{(j)}(V) = k_B \rho_a^{(j)} \left[\left(1 + \frac{n_h^{(j)}(V)}{\rho_a^{(j)}} \right) \ln \left(1 + \frac{n_h^{(j)}(V)}{\rho_a^{(j)}} \right) - \frac{n_h^{(j)}(V)}{\rho_a^{(j)}} \ln \left(\frac{n_h^{(j)}(V)}{\rho_a^{(j)}} \right) \right]. \tag{5}$$

Here, ρ_a expresses the local density of the accessible microscopic states, which is determined by

$$\rho_a^{(j)} = \begin{cases} \dfrac{\mathrm{sgn}(k_{z0})}{8\pi^3}\mathrm{Re}\left[\dfrac{(1+R_1^{(j)}R_2^{(j)}e^{i2k_{z0}d}+\dfrac{k_\rho^2}{k_0^2}R_2^{(j)}e^{i2k_{z0}d_2}+\dfrac{k_\rho^2}{k_0^2}R_1^{(j)}e^{i2k_{z0}d_1})}{1-R_1^{(j)}R_2^{(j)}e^{i2k_{z0}d}}\right] & \text{for PW,} \\ \dfrac{\mathrm{sgn}(\beta_{z0})}{8\pi^3}\dfrac{k_0}{\sqrt{\beta_{z0}^2+k_\rho^2}} & \\ \times\mathrm{Im}\left[\dfrac{(1+R_1^{(j)}R_2^{(j)}e^{-2\beta_{z0}d}+\dfrac{k_\rho^2}{k_0^2}R_2^{(j)}e^{-2\beta_{z0}d_2}+\dfrac{k_\rho^2}{k_0^2}R_1^{(j)}e^{-2\beta_{z0}d_1})}{1-R_1^{(j)}R_2^{(j)}e^{-2\beta_{z0}d}}\right] & \text{for EW.} \end{cases} \tag{6}$$

2.3. Thermodynamic bounds of the cooling power densities and efficiency

To evaluate the performance of the near-field EL and NEL systems, we assume that the EL device and the heat source have the same temperature ($T_{EL} = T_1$) since the flux of heat conduction is usually much larger than that of thermal radiation, especially when the temperature is below 300 K. Similarly, the temperature of the NEL device is the same as the temperature of the heat sink ($T_{NEL} = T_2$). Then we get the thermodynamic bounds of the cooling power densities P and the COP of the EL and NEL systems when the systems are assumed to be operating in the ultimate case and there is no entropy generated in the EL or NEL devices ($S_{gen} = 0$), therefore $S_C = S_1 - S_2$.

For the EL system, P_{EL} and COP bound can be expressed as

$$P_{EL} = Q_C = T_1 \times S_C = T_1 \times (S_1 - S_2). \tag{7}$$

$$\begin{aligned} \eta_{EL} &= \frac{P_{EL}}{W} = \frac{Q_C}{(E_1 - E_2) - Q_C} = \frac{T_1 \times S_C}{(E_1 - E_2) - T_1 \times S_C} \\ &= \frac{T_1 \times (S_1 - S_2)}{(E_1 - E_2) - T_1 \times (S_1 - S_2)}. \end{aligned} \tag{8}$$

For the NEL system, P_{NEL} and COP bound are determined by

$$P_{NEL} = E_1 - E_2. \tag{9}$$

$$\begin{aligned} \eta_{NEL} &= \frac{P_{NEL}}{W} = \frac{E_1 - E_2}{Q_C - (E_1 - E_2)} = \frac{E_1 - E_2}{T_2 \times S_C - (E_1 - E_2)} \\ &= \frac{E_1 - E_2}{T_2 \times (S_1 - S_2) - (E_1 - E_2)}. \end{aligned} \tag{10}$$

It is worth to note that for the EL device, the main part of the input entropy is carried by the thermal conduction, but the output entropy is purely carried by the thermal radiation, as shown in Figure 1. And for the NEL device, the entropy is input by the thermal radiation and output by the thermal conduction. However, the entropy to energy ratio of thermal conduction ($1/T$) is different from that of thermal radiation [67]. Thus, our results do show the deviation from the Carnot limit.

3. Results and discussion

3.1. Near-field enhancement on the EL and NEL systems

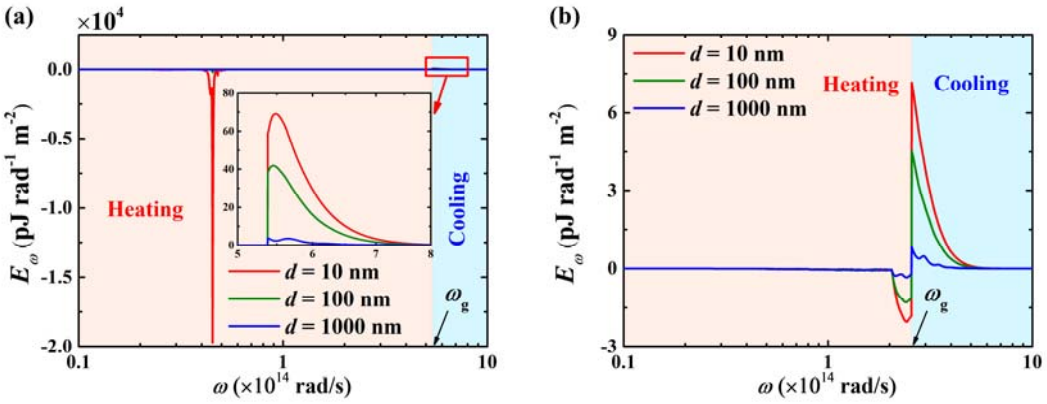

Figure 2. (a) Spectral radiative heat flux for an applied voltage of 0.2 V in the EL system. (b) Spectral radiative heat flux for an applied voltage of – 0.2 V in the NEL system. The cooling target temperature T_1 = 290 K and the red, green, and blue curves are for d = 10, 100, and 1000 nm, respectively.

We first focus on the performance of the near-field EL and NEL systems at different vacuum gaps for the heat source of the EL system and the emitter of the NEL system at a cooling target temperature T_1 = 290 K. In Figure 2, we plot the spectral radiative energy flux for an applied voltage of 0.2 V in the EL system and – 0.2 V in the NEL system, respectively. For both systems, it can be seen that in the region where the frequency is below ω_g, the radiative heat transfer is negative due to the temperature difference when the chemical potential of photons below the bandgap is zero. In the high-frequency region, the non-zero chemical potential provided by the applied voltage of the EL and NEL devices produces a positive heat transfer, thus resulting in a refrigeration effect, as shown in Figure 2. Moreover, the absolute heat flux increases greatly as the vacuum gap reduces in the entire frequency region for both EL and NEL systems. This effect is typical for near-field radiative heat transfer where the transferred heat flux can be significantly enhanced as the gap distance between the two bodies decreases. The corresponding spectral entropy flux curves show a similar trend with the spectral heat flux curves, but they are more than two orders of magnitude lower, as shown in Figure 3.

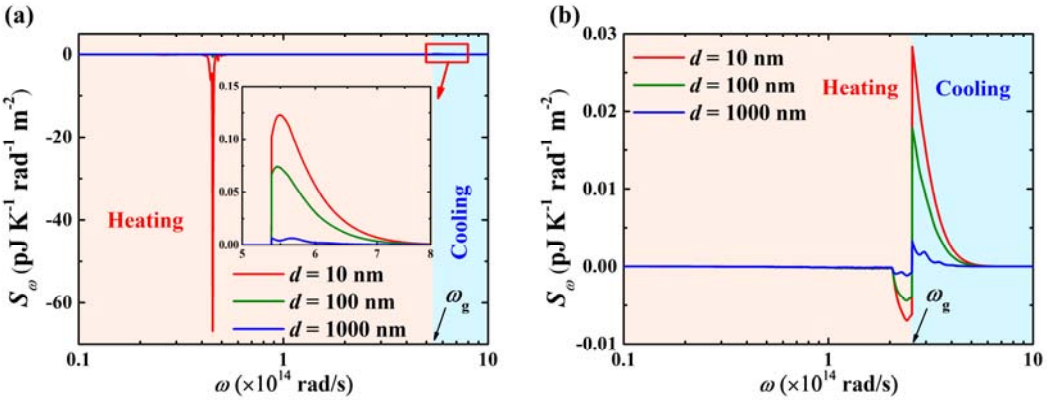

Figure 3. (a) Spectral radiative entropy flux for an applied voltage of 0.2 V in the EL system. (b) Spectral radiative energy flux for an applied voltage of –0.2 V in the NEL system. The cooling target temperature $T_1 = 290$ K and the red, green, and blue curves are for $d = 10$, 100, and 1000 nm, respectively.

The physical origins of the spectral radiative energy flux can be better illustrated by examining the energy transmission coefficient as a function of ω and β. Figure 4(a) displays the contour plot of the transmission coefficient of the EL system for $d = 10$ nm. Note that due to the sum of both s and p polarizations the maximum transmission coefficient is 2. The bright color indicates a high transmission coefficient. In the above-bandgap frequency range, InAs exhibits significant absorption since it is a direct bandgap material. In the frequency range below the InAs bandgap, the surface phonon polaritons (SPhPs) of InAs clearly cause a heat flux peak around 0.45×10^{14} rad/s as can be identified in Figure 4(a). Since InAs is a polar material, the real part of the dielectric function Re(ε) changes from positive to negative around the optical phonon frequency. The SPhPs can be excited and contribute significantly to radiative heat transfer at the frequency where Re(ε) is – 1. The contour plot of the transmission coefficient of the NEL system for $d = 10$ nm is shown in Figure 4(b), it is found that no surface mode could be excited between two MCT films in the frequency range below the bandgap.

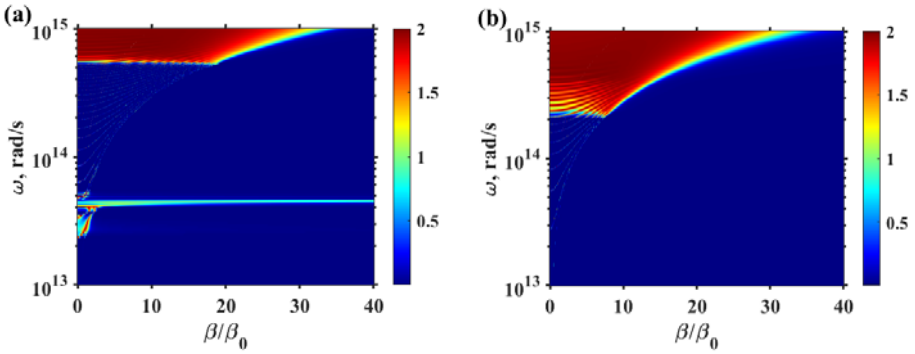

Figure 4. Contour plots of the energy transmission coefficient of (a) the EL system and (b) the NEL system, respectively, when $d = 10$ nm. Wavevector β is normalized by $\beta_0 = \omega_0/c$ with $\omega_0 = 10^{14}$ rad/s.

In Figure 5(a) we plot the integrated cooling power density of the EL system as a function of the applied voltage for vacuum gap d = 10, 100, 1000 nm, respectively. When the applied voltage $V_{EL} = 0$, the cooling power density $P_{EL} < 0$ at every vacuum gap d, which means that there is net heat flux from the hot absorber to the cold EL device because of the negative thermal radiation caused by the temperature difference. With the applied voltage V_{EL} increases, the heat flux from the EL device increases so slowly. As V_{EL} continues to increase, P_{EL} increases approximately exponentially. At d = 10 nm, we see that the cooling power density P_{EL} stays negative at any V_{EL}. It can be observed from Figure 2(a), in the near-field, the sub-bandgap thermal radiation accounts for the main part of the heat transfer between the EL device and the absorber, and hence the cooling effect does not appear in the range of applied voltage we considered. Whereas for an intermediate vacuum gap d = 100 nm, as V_{EL} increases beyond a threshold voltage of 0.136 V, the cooling power density P_{EL} becomes positive and the EL device appears a net outflow of heat and hence cooling. The maximum P_{EL} reaches 1289 W/m^2 at V_{EL} = 0.2 V. As the vacuum gap further increases to 1000 nm, a much lower cooling power density can also be achieved, with a maximum P_{EL} of 106 W/m^2 at V_{EL} = 0.2 V.

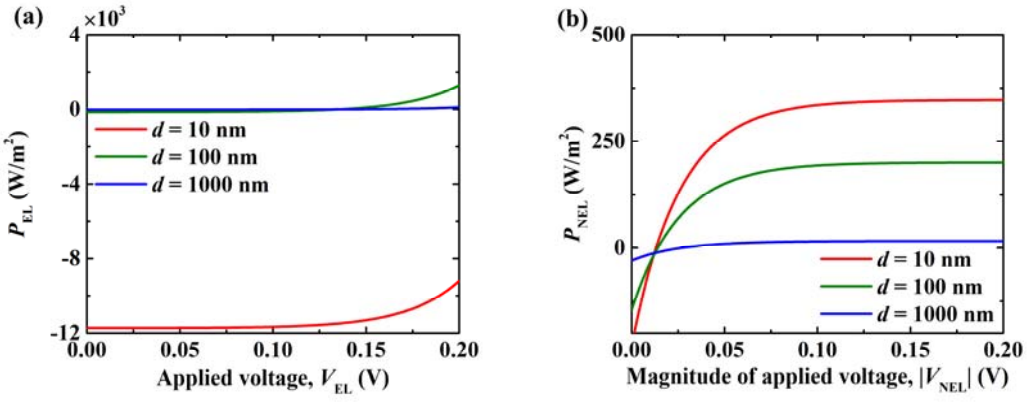

Figure 5. The cooling power density as a function of the applied voltage V_{EL} or the magnitude of voltage $|V_{NEL}|$ for different vacuum gaps d in (a) the EL system and (b) the NEL system at T_1 = 290 K. The red, green, and blue curves are for d = 10, 100, and 1000 nm, respectively.

Then we plot the cooling power density of the NEL system in Figure 5(b). For each vacuum gap d, P_{NEL} is negative at $V_{NEL} = 0$, then it increases dramatically and becomes positive as the magnitude of applied reverse voltage $|V_{NEL}|$ increases due to the lower bandgap of the MCT which leads to the predominant above-bandgap heat transfer. Unlike the EL system, the cooling power density of the NEL system slows down gradually and finally reaches saturation and no longer increases markedly, because when $|V_{NEL}|$ is large enough, the heat flux from the biased NEL device is insignificant compared to the heat flux from the emitter. Besides, as d decreases, P_{NEL} can also be greatly enhanced due to the near-field effects, we note that the maximum P_{NEL} increases about 22 times, from 16 to 347 W/m^2 as the vacuum gap decreases from 1000 to 10 nm at $V_{NEL} = -0.2$ V.

The COP bounds versus the voltage of the EL and NEL systems are given in Figure 6(a) and (b), respectively. We note that the vacuum gap plays an important role in the COP bounds of both refrigeration systems. For the EL system, the COP bound is zero when the applied voltage V_{EL} is small

since the cooling power density P_{EL} is negative. As V_{EL} increases to exceed the threshold voltage, the COP bound quickly increases to a maximum value and then decreases as V_{EL} further increases. The maximum COP bound reaches 1.19 at V_{EL} = 0.176 V for d = 100 nm and 1.10 at = 0.182 V for d = 1000 nm.

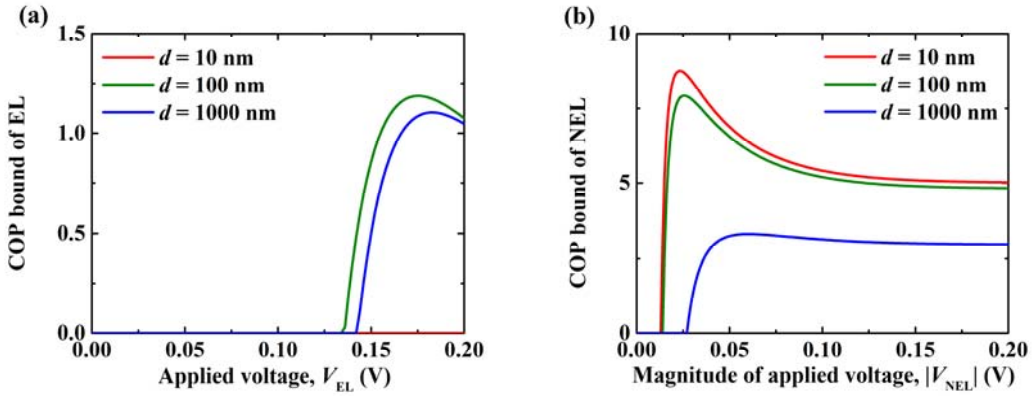

Figure 6. COP bound as a function of the applied voltage V_{EL} or the magnitude of voltage $|V_{NEL}|$ at different vacuum gaps d in (a) the EL system and (b) the NEL system at T_1 = 290 K. The red, green, and blue curves are for d = 10, 100, and 1000 nm, respectively.

For the NEL system, the COP bound is zero at the magnitude of applied voltage $|V_{NEL}|$ below the threshold voltage since the applied voltage is too weak to suppress the thermal radiation from the semiconductor NEL device. After that, it rapidly increases to the maximum value at $|V_{NEL}|$ slightly above the threshold voltage and then decreases as $|V_{NEL}|$ further increases. When the vacuum gap d = 1000 and 100 nm, the maximum COP bound is 3.3 and 7.9 respectively, which is much larger than that of the EL system under the same conditions. Further reducing the vacuum gap to 10 nm, the maximum COP bound reaches 8.76 at V_{NEL} = – 0.023 V. Moreover, the saturation of the COP bound of the NEL system is 5.0 at d = 10 nm, 4.8 at d = 100 nm, and 2.9 at d = 1000 nm.

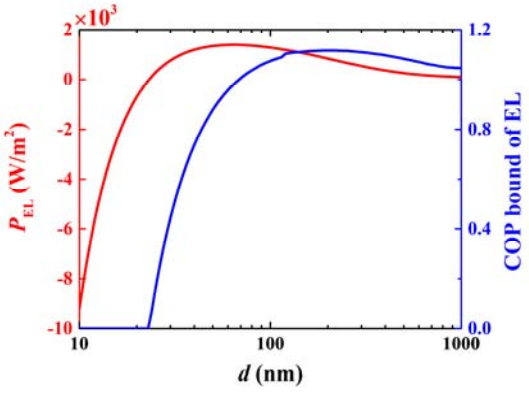

Figure 7. The cooling power density and the COP bound of the EL system as a function of the vacuum gaps d for applied voltage V_{EL} = 0.2 V at T_1 = 290 K.

Based on the above analysis, for the EL system, it can be found that the cooling power density P_{EL} and the COP bound do not always increase with decreasing the vacuum gap d. Thus, there should be an optimized d between 10 and 1000 nm that maximizes P_{EL} and the COP bound of the EL system. Figure 7 gives the cooling power density and the COP bound as a function of the vacuum gap at an applied voltage of 0.2 V. The cooling power density P_{EL} is negative at vacuum gap $d < 24$ nm since the sub-bandgap thermal radiation dominates over the above-bandgap thermal radiation. With the increase of d, P_{EL} increases rapidly and reaches the maximum of 1398 W/m^2 at $d = 63.1$ nm. Further increasing d, P_{EL} decreases and stabilizes gradually. The COP bound also increases quickly first, and then it decreases as d increases. The maximum COP bound is 1.1 and is found at $d = 200$ nm.

3.2. Effects of the temperature difference

In the above section, the cooling target temperatures T_1 is set to 290 K, whereas high-temperature T_2 is assumed to be fixed at 300 K. Of course, the temperature difference $\Delta T = T_2 - T_1$ could be higher by decreasing T_1. Figure 8 compares the cooling power densities of near-field EL and NEL systems at temperature difference $\Delta T = 10$, 20, and 30 K. We set the vacuum gap $d = 100$ nm, which is easier to achieve in practice. At the same time, the EL system shows an acceptable cooling power density and COP at this vacuum gap.

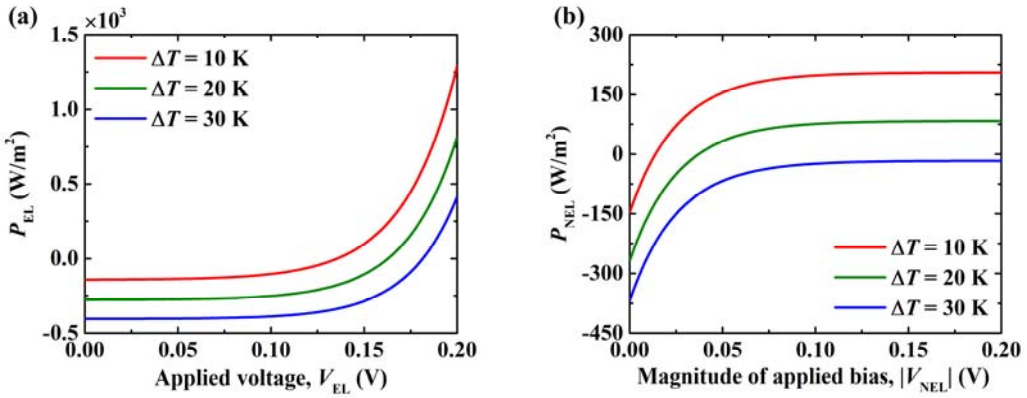

Figure 8. (a) The cooling power density as a function of the applied voltage V_{EL} at different temperature differences in the EL system. (b) The cooling power density as a function of the magnitude of voltage $|V_{NEL}|$ at different temperature differences in the NEL system. The vacuum gap $d = 100$ nm.

In terms of Eq (2), as temperature difference ΔT increases or cooling target temperature T_1 decreases, the photons emitted from the EL device of the EL system and the emitter of the NEL system decrease. As a result, it can be observed that the cooling power density decreases in both systems. As ΔT increases from 10 to 30 K, for the EL system, the maximum cooling power density P_{EL} for $d = 100$ nm at $V_{EL} = 0.2$ V decreases from 1289 to 414 W/m^2. On the other hand, for the NEL system, maximum P_{NEL} at $V_{NEL} = -0.2$ V decreases from 205 to 83 W/m^2 as ΔT increases from 10 to 20 K. In addition, the NEL system fails to achieve any cooling effect at $|V_{NEL}| < 0.2$ V when ΔT increases to 30 K.

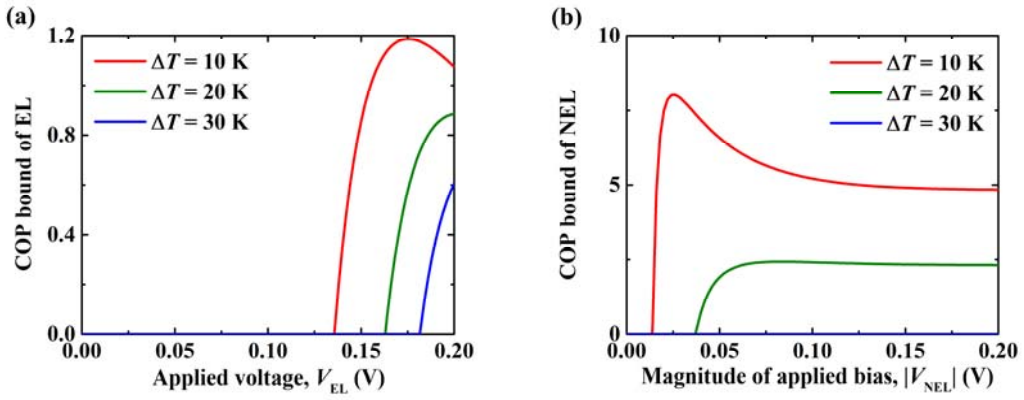

Figure 9. (a) COP bound as a function of the applied voltage V_{EL} at different temperature differences in the EL system. (b) COP bound as a function of the magnitude of voltage $|V_{NEL}|$ at different temperature differences in the NEL system. The vacuum gap d = 100 nm.

In Figure 9(a) and (b), we plot the COP bounds of near-field EL and NEL systems as a function of the applied voltage for various temperature differences ΔT, respectively. Similar to the cooling power density, we note that the COP bound also decreases in both EL and NEL systems as the temperature difference ΔT increases. For the near-field EL system, as ΔT increases from 10 to 30 K, the maximum COP bound decreases from 1.19 to 0.6. On the other hand, the COP bound of the NEL system shows a more drastic reduction as compared to that of the EL system. The saturation of the COP bound decreases from 4.8 to 2.3 as ΔT increases from 10 to 20 K. We also mention that the threshold voltage for achieving the refrigeration effect (positive P) increases as the temperature difference ΔT goes up in both systems because a higher chemical potential is needed to overcome the increased temperature differences.

By comparing the EL and NEL systems from Figures 8 and 9, it is found that the EL system can reach higher cooling power density and temperature difference. However, the NEL system can achieve a refrigeration effect at a lower voltage and temperature difference with a higher COP.

3.3. Ideal cases without considering the sub-bandgap thermal radiation

In the above sections, we demonstrate that the EL and NEL systems shown in Figure 1 can work as cooling devices with considerable cooling power density and COP bound. However, in this near-field regime, the presence of sub-bandgap thermal radiation can become very substantial. For both EL and NEL cooling systems, such thermal radiation represents a disadvantage since it results in undesired and detrimental heat flux from the hot heat reservoir to the cold cooling target. In order to evaluate the adverse effects of the sub-bandgap thermal radiation and provide suggestions for system performance improvement. In this section, we evaluate the performance of the ideal EL and NEL refrigeration systems in the absence of sub-bandgap heat transfer.

Figure 10 shows the integrated cooling power density as a function of applied voltage V_{EL} or the magnitude of negative applied voltage $|V_{NEL}|$ for different vacuum gaps d = 10, 100, and 1000 nm, respectively. For both the EL and NEL system, the absence of sub-bandgap thermal radiation enhances the cooling power density for all three cases significantly. Completely different from

Figure 5(a), the heat flux P_{EL} at d = 10 nm becomes positive and the maximum value reaches 2536 W/m^2 at V_{EL} = 0.2 V. And the stationary P_{NEL} increases by 28% at d = 10 nm and 123% at d = 1000 nm without the consideration of sub-bandgap thermal radiation. We also find that the cooling power density of an EL system increases significantly as the vacuum gap d decreases. The maximum cooling power density P_{EL} is 122 W/m^2 at the applied voltage of 0.2 V for d = 1000 nm. For comparison, we note that the maximum P_{EL} at d = 10 nm for this system can be increased by about 21 times to 2536 W/m^2 at the same applied voltage. Besides, for the NEL system, the maximum P_{NEL} increases about 12 times, from 36 to 445 W/m^2 as the vacuum gap decreases from 1000 to 10 nm at V_{NEL} = − 0.2 V.

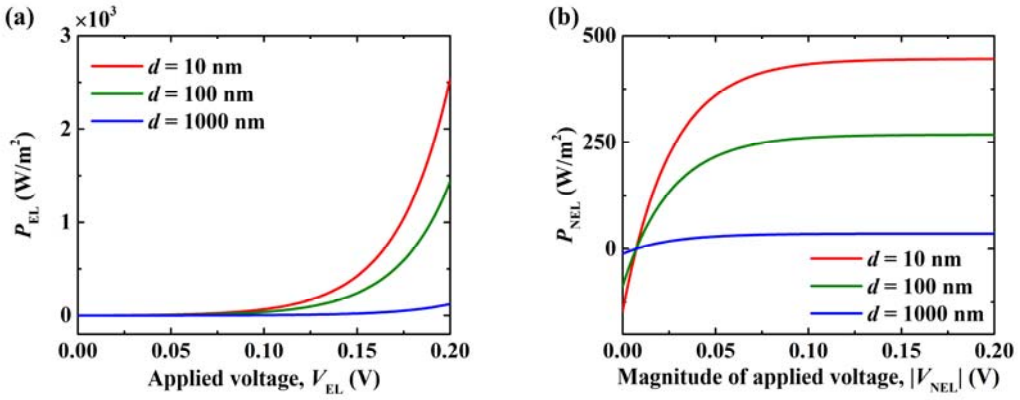

Figure 10. (a) The cooling power density as a function of the applied voltage V_{EL} at different vacuum gaps d in the EL system. (b) The cooling power density as a function of the magnitude of voltage $|V_{NEL}|$ at different vacuum gaps d in the NEL system. The cooling target temperature T_1 = 290 K and the red, green, and blue curves are for d = 10, 100, and 1000 nm, respectively.

Then we show the COP bound of the near-field EL system as a function of applied voltage for three vacuum gaps d in Figure 11(a). For all vacuum gaps, we observe that the COP bounds of the EL systems exhibit nearly identical curves. This phenomenon is because the near-field effects can enhance both the heat flux and entropy flux, according to Eq (8), the vacuum gap plays little role in the COP. The COP bound is zero when the applied voltage V_{EL} is small since the cooling power density P_{EL} is negative. Then the COP bound increases rapidly and reaches a maximum at V_{EL} slightly above the threshold voltage. It is found that an ideal EL system exhibits a maximum COP bound of 26.2 at V_{EL} = 0.014 V when the vacuum gap d = 10 nm, which is close to 29 of the Carnot limit ($T_1 / (T_2 - T_1)$). Finally, the COP bound gradually decreases and approaches zero as V_{EL} further increases.

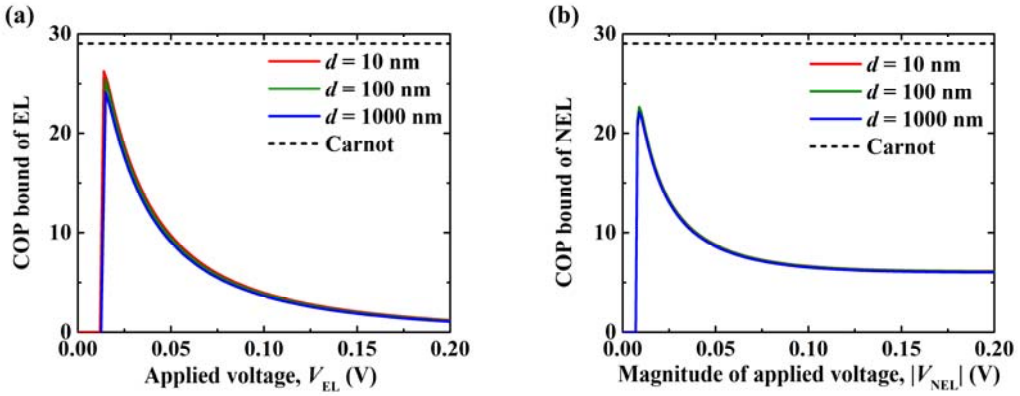

Figure 11. (a) COP bound as a function of the applied voltage V_{EL} at different vacuum gaps d in the EL system. (b) COP bound as a function of the magnitude of voltage $|V_{NEL}|$ at different vacuum gaps d in the NEL system. The cooling target temperature $T_1 = 290$ K and the red, green, and blue curves are for d = 10, 100, and 1000 nm, respectively. The horizontal dashed lines represent the Carnot efficiency limit.

The obtained COP bound for the NEL system is shown in Figure 11(b). Similar to that in Figure 10(a), the vacuum gap almost makes no difference to the COP bound of NEL systems. For all three vacuum gaps, the COP bound is zero at the magnitude of applied voltage $|V_{NEL}| < 0.008$ V since the applied voltage is too weak to suppress the thermal radiation from the semiconductor NEL device. After that, it rapidly increases to the maximum value at $|V_{NEL}|$ slightly above the threshold voltage and then decreases as $|V_{NEL}|$ further increases. The maximum COP bound is 21, which is lower than that of the EL system. Unlike the COP bound of the EL system, it can be observed that as $|V_{NEL}|$ further increases, the COP bound of the NEL system tends to stabilize at 6.1.

Based on the above results, it can be found that the sub-bandgap heat transfer weakens the cooling power densities and COP bounds of the EL and NEL systems tremendously. Therefore, to improve the performance of these two refrigeration systems, it is necessary to suppress the sub-bandgap heat transfer through optimization of structures and materials.

4. Conclusions

In summary, this study presents the thermodynamic limits for the performance of near-field EL and NEL refrigeration systems. It is shown how the cooling power density and COP bounds can be obtained from the formulation of thermodynamics by using the radiative heat flux and entropy flux considering near-field effects. The results show that the near-field effects are positive for the performance of the NEL systems. Indeed, we observe an enhancement of the maximum cooling power density by a factor of 22 for the NEL system as the vacuum gap decreases from 1000 nm to 10 nm. But the near-field effects are not always beneficial for the EL system, the cooling power density achieves the maximum of 1398 W/m^2 at d = 63.1 nm and the maximum COP bound reaches 1.1 at d = 200 nm in the EL system. Moreover, as the temperature difference increases or low cooling target temperature, the cooling power densities and the COP bounds of the EL and NEL systems both decrease significantly. Finally, the absence of the sub-bandgap thermal radiation enhances the

performance of both ideal refrigeration systems greatly. The COP bounds of the EL and NEL systems can be close to the Carnot limit. This study could pave the way toward providing fundamental bounds on the cooling power density and COP of near-field EL and NEL systems. And the results obtained here would present valuable guidance for improving the performance of these two systems.

Acknowledgments

This work was mainly supported by the National Natural Science Foundation of China (51776078, 51676077, 51827808, 51806070), the Fundamental Research Funds for the Central Universities (2019kfyXKJC033), the China Postdoctoral Science Foundation (2018M632849).

Conflict of interest

The authors declare that there are no conflicts of interest regarding the publication of this paper.

References

1. Polder D, Van Hove M (1971) Theory of Radiative Heat Transfer between Closely Spaced Bodies. *Phys Rev B* 4: 3303–3314.
2. Loomis JJ, Maris HJ (1994) Theory of heat transfer by evanescent electromagnetic waves. *Phys Rev B* 50: 18517–18524.
3. Pendry JB (1999) Radiative exchange of heat between nanostructures. *J Phys-Condens Mat* 11: 6621–6633.
4. Fu CJ, Zhang ZM (2006) Nanoscale radiation heat transfer for silicon at different doping levels. *Int J Heat Mass Tran* 49: 1703–1718.
5. Volokitin AI, Persson BNJ (2007) Near-field radiative heat transfer and noncontact friction. *Rev Mod Phys* 79: 1291–1329.
6. Hu L, Narayanaswamy A, Chen X, et al. (2008) Near-field thermal radiation between two closely spaced glass plates exceeding Planck's blackbody radiation law. *Appl Phys Lett* 92: 133106.
7. Basu S, Zhang ZM, Fu CJ (2009) Review of near-field thermal radiation and its application to energy conversion. *Int J Energ Res* 33: 1203–1232.
8. Rousseau E, Siria A, Jourdan G, et al. (2009) Radiative heat transfer at the nanoscale. *Nat Photonics* 3: 514–517.
9. Shen S, Narayanaswamy A, Chen G (2009) Surface Phonon Polaritons Mediated Energy Transfer between Nanoscale Gaps. *Nano Lett* 9: 2909–2913.
10. Qu W, Mudawar I (2002) Experimental and numerical study of pressure drop and heat transfer in a single-phase micro-channel heat sink. *Int J Heat Mass Tran* 45: 2549–2565.
11. Kittel A, Muller-Hirsch W, Parisi J, et al. (2005) Near-field heat transfer in a scanning thermal microscope. *Phys Rev Lett* 95: 224301.
12. Ottens RS, Quetschke V, Wise S, et al. (2011) Near-field radiative heat transfer between macroscopic planar surfaces. *Phys Rev Lett* 107: 014301.
13. St-Gelais R, Guha B, Zhu L, et al. (2014) Demonstration of strong near-field radiative heat transfer between integrated nanostructures. *Nano Lett* 14: 6971–6975.

14. Song B, Fiorino A, Meyhofer E, et al. (2015) Near-field radiative thermal transport: From theory to experiment. *Aip Adv* 5: 053503.
15. Laroche M, Carminati R, Greffet JJ (2006) Near-field thermophotovoltaic energy conversion. *J Appl Phys* 100: 063704.
16. Svetovoy VB, Palasantzas G (2014) Graphene-on-Silicon near-field thermophotovoltaic cell. *Phys Rev Appl* 2: 034006
17. Chang JY, Yang Y, Wang LP (2015) Tungsten nanowire based hyperbolic metamaterial emitters for near-field thermophotovoltaic applications. *Int J Heat Mass Tran* 87: 237–247.
18. Lenert A, Bierman DM, Nam Y, et al. (2014) A nanophotonic solar thermophotovoltaic device. *Nat Nanotechnol* 9: 126–130.
19. Fiorino A, Zhu L, Thompson D, et al. (2018) Nanogap near-field thermophotovoltaics. *Nat Nanotechnol* 13: 806–811.
20. Lin C, Wang B, Teo KH, et al. (2017) Near-field enhancement of thermoradiative devices. *J Appl Phys* 122: 143102.
21. Wang B, Lin C, Teo KH, et al. (2017) Thermoradiative device enhanced by near-field coupled structures. *J. Quant Spectros Radiat Transfer* 196: 10–16.
22. Liao T, Zhang X, Yang Z, et al. (2019) Near-Field Thermoradiative Electron Device. *IEEE Trans Electron Devices* 66: 3099–3102.
23. Chen K, Santhanam P, Sandhu S, et al. (2015) Heat-flux control and solid-state cooling by regulating chemical potential of photons in near-field electromagnetic heat transfer. *Phys Rev B* 91: 134301.
24. Liu X, Zhang ZM (2016) High-performance electroluminescent refrigeration enabled by photon tunneling. *Nano Energy* 26: 353–359.
25. Liao T, Tao C, Chen X, et al. (2019) Parametric optimum design of a near-field electroluminescent refrigerator. *J Phys D: Appl Phys* 52: 325108.
26. Chen K, Santhanam P, Fan S (2016) Near-Field enhanced negative luminescent refrigeration. *Phys Rev Appl* 6: 024014.
27. Lin C, Wang B, Teo KH, et al. (2018) A coherent description of thermal radiative devices and its application on the near-field negative electroluminescent cooling. *Energy* 147: 177–186.
28. Zhou C, Zhang Y, Qu L, et al. (2020) Near-field negative electroluminescent cooling via nanoparticle doping. *J Quant Spectrosc Radiat Transfer* 245: 106889–106897.
29. Wurfel P (1982) The chemical potential of radiation. *J Phys C Solid State Phys* 15: 3967.
30. Tervo E, Bagherisereshki E, Zhang Z (2017) Near-field radiative thermoelectric energy converters: a review. *Front Energy* 12: 5–21.
31. Tauc J (1957) The share of thermal energy taken from the surroundings in the electro-luminescent energy radiated from a p-n junction. *Cechoslovackij Fiziceskij Zurnal* 7: 275–276.
32. Dousmanis G, Mueller C, Nelson H, et al. (1964) Evidence of refrigerating action by means of photon emission in semiconductor diodes. *Phys Rev* 133: A316–A318.
33. Berdahl P (1985) Radiant refrigeration by semiconductor diodes. *J Appl Phys* 58: 1369–1374.
34. Mal'Shukov A, Chao K (2001) Opto-thermionic refrigeration in semiconductor heterostructures. *Phys Rev Lett* 86: 5570.
35. Han P, Jin KJ, Zhou YL, et al. (2006) Analysis of optothermionic refrigeration based on semiconductor heterojunction. *J Appl Phys* 99: 074504.

36. Yen ST, Lee KC (2010) Analysis of heterostructures for electroluminescent refrigeration and light emitting without heat generation. *J Appl Phys* 107: 054513.
37. Oksanen J, Tulkki J (2010) Thermophotonic heat pump—a theoretical model and numerical simulations. *J Appl Phys* 107: 093106.
38. Santhanam P, Huang D, Gray Jr DJ, et al. (2013) Electro-luminescent cooling: light emitting diodes above unity efficiency. *Laser Refrigeration of Solids VI*, 863807.
39. Santhanam P, Gray DJ Jr, Ram RJ (2012) Thermoelectrically pumped light-emitting diodes operating above unity efficiency. *Phys Rev Lett* 108: 097403.
40. Guha B, Otey C, Poitras CB, et al. (2012) Near-field radiative cooling of nanostructures. *Nano Lett* 12: 4546–4550.
41. Bewley WW, Jurkovic MJ, Felix CL, et al. (2001) HgCdTe photodetectors with negative luminescent efficiencies >80%. *Appl Phys Lett* 78: 3082–3084.
42. Nash GR, Ashby MK, Lindle JR, et al. (2003) Long wavelength infrared negative luminescent devices with strong Auger suppression. *J Appl Phys* 94: 7300–7304.
43. Ashley T, Gordon NT, Nash GR, et al. (2001) Long-wavelength HgCdTe negative luminescent devices. *Appl Phys Lett* 79: 1136–1138.
44. Hoffman D, Hood A, Wei Y, et al. (2005) Negative luminescence of long-wavelength InAs⁄GaSb superlattice photodiodes. *Appl Phys Lett* 87: 201103.
45. Ashley T, Elliott CT, Gordon NT, et al. (1995) Negative luminescence from $In_{1-x}Al_xSb$ and $Cd_xHg_{1-x}Te$ diodes. *Infrared Phys Technol* 36: 1037–1044.
46. Zhu L, Fiorino A, Thompson D, et al. (2019) Near-field photonic cooling through control of the chemical potential of photons. *Nature* 566: 239–244.
47. Rawat R, Lamba R, Kaushik SC (2017) Thermodynamic study of solar photovoltaic energy conversion: An overview. *Renewable Sustainable Energy Rev* 71: 630–638.
48. Ruan XL, Rand SC, Kaviany M (2007) Entropy and efficiency in laser cooling of solids. *Phys Rev B* 75: 214304.
49. Hsu WC, Tong JK, Liao B, et al. (2016) Entropic and near-field improvements of thermoradiative cells. *Sci Rep* 6: 34837.
50. Gribik J, Osterle J (1984) The second law efficiency of solar energy conversion. *J Sol Energy Eng* 106: 16–21.
51. Pusch A, Gordon JM, Mellor A, et al. (2019) Fundamental efficiency bounds for the conversion of a radiative heat engine's own emission into work. *Phys Rev Appl* 12: 064018.
52. Li W, Buddhiraju S, Fan S (2020) Thermodynamic limits for simultaneous energy harvesting from the hot sun and cold outer space. *Light Sci Appl* 9: 68.
53. Dorofeyev I (2011) Thermodynamic functions of fluctuating electromagnetic fields within a heterogeneous system. *Phys Scr* 84: 055003.
54. Perez-Madrid A, Lapas LC, Rubi JM (2009) Heat exchange between two interacting nanoparticles beyond the fluctuation-dissipation regime. *Phys Rev Lett* 103: 048301.
55. Pérez-Madrid A, Rubí JM, Lapas LC (2008) Heat transfer between nanoparticles: Thermal conductance for near-field interactions. *Phys Rev B* 77: 155417
56. Latella I, Pérez-Madrid A, Lapas LC, et al. (2014) Near-field thermodynamics: Useful work, efficiency, and energy harvesting. *J Appl Phys* 115: 124307.
57. Narayanaswamy A, Zheng Y (2013) Theory of thermal nonequilibrium entropy in near-field thermal radiation. *Phys Rev B* 88: 075412.

58. Li B, Cheng Q, Song J, et al. (2020) Evaluation of performance of near-field thermophotovoltaic systems based on entropy analysis. *J Appl Phys* 127: 063103.
59. Ravindra NM, Srivastava VK (1979) Temperature dependence of the energy gap in semiconductors. *J Phys Chem Solids* 40: 791–793.
60. Palik ED (1985) Handbook of Optical Constants of Solids, Orlando: Academic Press.
61. Johnson PB, Christy RW (1972) Optical Constants of the Noble Metals. *Phys Rev B* 6: 4370–4379.
62. Kruger M, Emig T, Kardar M (2011) Nonequilibrium electromagnetic fluctuations: heat transfer and interactions. *Phys Rev Lett* 106: 210404.
63. Otey C, Fan S (2011) Numerically exact calculation of electromagnetic heat transfer between a dielectric sphere and plate. *Phys Rev B* 84: 245431.
64. Chew WC (1995) Waves and Fields in Inhomogeneous Media, New York: IEEE.
65. Basu S, Lee BJ, Zhang ZM (2010) Infrared radiative properties of heavily doped silicon at room temperature. *J Heat Transfer* 132: 023301.
66. Smith GB (1990) Theory of angular selective transmittance in oblique columnar thin films containing metal and voids. *Appl Opt* 29: 3685–3693.
67. Zhang Z (2007) Nano/microscale heat transfer, New York: McGraw-Hill.

AIMS Press